

**This is an electronic reprint of the original article.
This reprint *may differ* from the original in pagination and typographic detail.**

Author(s): Bazhenova, Elena; Honkala, Karoliina

Title: Screening the bulk properties and reducibility of Fe-doped Mn₂O₃ from first principles calculations

Year: 2017

Version:

Please cite the original version:

Bazhenova, E., & Honkala, K. (2017). Screening the bulk properties and reducibility of Fe-doped Mn₂O₃ from first principles calculations. *Catalysis Today*, 285, 104-113.
<https://doi.org/10.1016/j.cattod.2017.02.004>

All material supplied via JYX is protected by copyright and other intellectual property rights, and duplication or sale of all or part of any of the repository collections is not permitted, except that material may be duplicated by you for your research use or educational purposes in electronic or print form. You must obtain permission for any other use. Electronic or print copies may not be offered, whether for sale or otherwise to anyone who is not an authorised user.

Screening the bulk properties and reducibility of Fe-doped Mn₂O₃ from first principles calculations

Elena Bazhenova^a, Karoliina Honkala^{a,*}

^aNanoscience Center, Department of Chemistry, University of Jyväskylä, P.O.box 35, FI-40014 Jyväskylä, Finland

*Corresponding author at: Nanoscience Center, Department of Chemistry, University of Jyväskylä, P.O.box 35, FI-40014 Jyväskylä, Finland. Tel.: +358 408053686
E-mail address: karoliina.honkala@jyu.fi

ABSTRACT

Manganese oxides, particularly Mn₂O₃, have demonstrated great potential for oxygen carrier materials in chemical looping applications. The application of these materials in the industrial scale is hindered by thermodynamic restrictions related to the reoxidation process. This disadvantage can be overcome by doping the oxide with a guest cation. Iron is one of the most promising dopants but the atomic-level understanding of its effects on the properties of α-Mn₂O₃ is incomplete. Herein, we report a systematic GGA+U study of the bulk properties and reducibility of Fe_xMn_{2-x}O₃ (0 ≤ x ≤ 2) as a function of Fe dopant concentration. In particular, we focus on a representative set of 20 models with different Fe content, generated by screening several thousand structures. Our results indicate that substitution of Mn atoms with Fe stabilizes Fe_xMn_{2-x}O₃, which is visible through negative values of doping energies, decreasing oxide formation energies, and higher oxygen vacancy formation energies with increasing Fe concentration. Similar to Fe, the presence of an oxygen vacancy increases the band gap in the major spin channel of Fe_xMn_{2-x}O₃. Oxygen transport in Fe_xMn_{2-x}O₃ is found to depend on Fe content and distribution in the lattice. All in all, our findings provide atomic-level insight into the properties of Fe_xMn_{2-x}O₃ and generally agree with experimental observations. Obtained information can be applied to investigate the reactivity of Fe_xMn_{2-x}O₃.

Key words

Density functional theory, Mn₂O₃, bulk, Fe dopants.

1. Introduction

Chemical Looping (CL) processes are an appealing technology offering an effective and versatile reduction-oxidation scheme to convert carbonaceous fuels into heat, electricity or hydrogen in large scale applications providing CO₂ capture at a low cost [1–3]. Requisite oxygen is supplied by a solid oxygen carrier, which acts as a redox catalyst. During the reduction step, the carrier donates oxygen, which is then used to oxidize a given reactant, leading to the formation of oxygen deficient carrier materials. In the following healing step, the carrier is filled in again with oxygen. This reloading takes place under oxygen atmosphere in a physically separate reactor.

The future success in CL applications depends sensitively on oxygen carrier materials, and thus significant research efforts have been put forward to design and develop suitable materials. The desirable properties of promising oxygen carrier materials include high oxygen-carrying capacity, high fuel conversion, good redox reactivity, and high thermal stability. Experimentally, Cu, Ni, Fe, Mn and Co-based oxides [4] are found to be most promising carrier materials for different CL applications [5,6]. These primary, active,

transition metal oxides are typically supported by an inert oxide such as ZrO_2 , Al_2O_3 , and SiO_2 [4]. Cu and Mn oxides demonstrate high activity for CL combustion processes [4] and Fe oxide, on the other hand, is found to be a promising redox catalyst for methane partial oxidation [3]. The usage of pure manganese oxides is thermodynamically limited due to problematic reoxidation of the oxide under operating temperature [7]. In other words, oxygen release takes place easily but the reoxidation of the reduced oxide is challenging. To improve oxygen uptake, Mn oxide is typically mixed with another oxide. This has been done for the following combinations of host and guest cations: Mn/Mg[8], Mn/Ni [9], Mn/Si [10,11], and Mn/Fe oxides [12–18]. Among the studied systems, Mn/Fe oxide has been found to be the most promising compromise between oxygen release and reoxidation [12–18].

While the properties of different oxygen carrier materials have been extensively explored experimentally, computational studies are scarce and they mainly focus on the properties of surfaces and supported clusters. Density functional theory calculations (DFT) employing both periodic [19,20] and cluster models [21] have been carried out for CO oxidation to CO_2 on α - Fe_2O_3 . The calculations show that on the (1102) surface of α - Fe_2O_3 CO prefers to adsorb on the O-top site forming CO_2 with lattice oxygen desorbing then with an activation energy of less than 20 kJ/mol. The carrier-support interactions have been explored computationally for CO oxidation at a MgO-supported Fe_2O_3 cluster [21]. The calculations show that the support increases the average Fe-O bond distance activating Fe_2O_3 for oxygen release. The computed activation energy for CO oxidation is about 158 kJ/mol lower on the supported cluster compared to a free-standing cluster. Improved CO adsorption has also been observed for Fe_2O_3 clusters supported on ZnO_2 and Al_2O_3 surfaces [22–24]. Another example of a computational study on carrier-support interactions deals with CuO/ZrO_2 and focused on sintering of Cu-oxide clusters and CO oxidation on the supported cluster [25]. According to calculations, the strong interaction between the CuO cluster and the ZrO_2 support hinders the migration of the cluster while simultaneously activating it towards CO oxidation. The activation energy for CO oxidation decreases from 139 kJ/mol on the unsupported cluster to 76 kJ/mol on the supported one. Recently, chemical looping reforming of methane on α - $Fe_2O_3(001)$ has been studied via DFT calculations [26]. On the stoichiometric α - $Fe_2O_3(001)$ surface, methane adsorption is found to be weak and the adsorption energy of the methane derived radical increases with decreasing number of H atoms. On the reduced surface, methane adsorption is even weaker than on the stoichiometric surface, while the adsorption strength of radicals significantly increases. Overall, the addition of an oxygen vacancy and stronger adsorption of radicals are proposed to promote oxidation of methane [26] and thus to improve the performance of α - Fe_2O_3 as an oxygen carrier.

Computational studies on α - Mn_2O_3 mainly focus on the bulk properties of the oxide, in particular the electronic structure and magnetic ordering [27,28]. Surface activity is considered for oxygen reduction and water oxidation [29]. The combined experimental and DFT investigation demonstrates the great potential of α - Mn_2O_3 as a bifunctional catalyst for oxygen reduction and oxygen evolution reactions, where the ability of an Mn ion to change its oxidation state from +3 to +4 is particularly important for the overall catalytic performance. Moreover, it is found that pH and the applied potential impact on the stability of an oxide surface and Mn_2O_3 experiences a phase transition under the certain conditions.

Although α - Fe_2O_3 and α - Mn_2O_3 have been previously addressed, computational studies on b - Fe_2O_3 and Fe-doped α - Mn_2O_3 are not available in the literature. However, atomic-level understanding how Fe dopants affect structural and electronic properties, and the reducibility of α - Mn_2O_3 would help to elucidate their behavior in CL applications.

Herein, we present a systematic evaluation of bulk properties and reducibility of $Fe_xMn_{2-x}O_3$ oxide as a function of their chemical composition employing density functional theory

calculations. We begin with screening several thousand structures and selecting a representative set of models for the doped oxide. For each selected structure, doping energy, oxide formation energy, and electronic and magnetic structures are carefully examined. Finally, we study the energy of vacancy formation and oxygen diffusion to address efficiency of redox kinetics, which is the central property of an oxygen carrier.

2. Methods and models

2.1. Computational details

Periodic electronic structure calculations were performed using the grid-based projector augmented plane wave approach, as implemented in GPAW 0.10.0 [30–32]. Wave functions were represented on a uniform real-space grid with the spacing of 0.16 Å. Within the GGA+U formalism, Perdew-Burke-Ernzerhof (PBE) exchange-correlation functional [33] was used together with the Hubbard U correction [34,35] of 4 eV [36] for both Mn and Fe atoms to account for strong on-site Coulomb interaction. Main results were tested against different U values for Mn and Fe d-orbitals. We found that changes in U values introduce small variations to calculated quantities such as band gaps and vacancy formation energies but the overall trends remain the same (see Supplementary material, Section 1). The Fermi smearing with the width of 0.2 eV was applied and all the calculations were performed at the Γ -point, which has been previously demonstrated to be a valid approach [37]. Atomic positions were always relaxed until maximum residual force was below 0.035 eV/Å. The impact of a tighter convergence criteria was found to be minor to the computed energy differences. The diffusion barrier was determined employing the Nudged Elastic Band (NEB) method [38] with the total number of images being 7.

2.2. Structures of pure and mixed oxides

Manganese (III) oxide exists in two forms, namely *a*-Mn₂O₃ and *g*-Mn₂O₃, which differ from each other in the symmetry of crystal. More importantly, the *g*-form dominates at low temperatures while *a*-Mn₂O₃ is more stable at high-temperature, CL, conditions [39,40]. In addition, the *a*-form can be further stabilized by replacing Mn cations in the lattice with Fe [39]. Therefore, we employed *a*-Mn₂O₃ throughout the current study. The *a*-Mn₂O₃ bulk belongs to the Ia3 space group and exhibits the bixbyite structure (Figure 1), where Mn atoms occupy 8 Wyckoff positions A and 24 Wyckoff positions D while O atoms occupy 48 Wyckoff positions E [41]. Note, that metal atoms occupying different Wyckoff positions differ in local symmetry operations [42] (atoms in position A have higher symmetry than atoms in position D), but have the same coordination and surroundings. Iron (III) oxide features a variety of different crystal structures: *a*-Fe₂O₃ (hematite) with space group R3c, *b*-Fe₂O₃ with space group Ia3, *g*-Fe₂O₃ (maghemite) with space group P2₁3, and *e*-Fe₂O₃ with space group Pna2₁. Even though the most common form Fe₂O₃ is *a*, the *b*-form is of a particular interest to the current study, as it is isomorphic to *a*-Mn₂O₃.

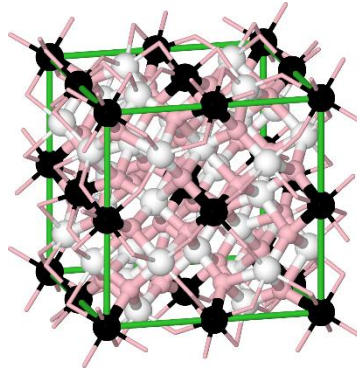


Figure 1. The computational cell of the bixbyite structure of α - Mn_2O_3 . Color indicates different Wyckoff positions: metal atoms at positions A are colored black, metal atoms at positions D are given in white, and oxygen atoms in positions E are represented in pink.

The atomic structure of $\text{Fe}_x\text{Mn}_{2-x}\text{O}_3$ oxide is very complex and depends on the preparation method, ambient conditions, and the relative concentrations of Mn and Fe atoms [12,14–17,43,44]. Bixbyite and hematite structures are predominant phases at low temperatures and which one of them dominates depends on the Mn/Fe ratio. In general, temperature increase leads to oxygen release and the formation of a spinel structure [14,15,43]. Powder diffraction studies for mixed oxides have demonstrated that the spectrums of systems with different Mn/Fe ratios present the typical peaks of Mn_2O_3 , Fe_2O_3 , and $\text{Fe}_x\text{Mn}_{(x-1)}\text{O}_3$ [16]. Moreover, all these systems have been identified to have a bixbyite structure. The gradual increase of Fe content up to 50 % in α - Mn_2O_3 does not impact the bixbyite structure, while at higher iron concentrations the additional hematite phase appears [12,17,44]. Existence of a b - Fe_2O_3 phase in $\text{Fe}_x\text{Mn}_{2-x}\text{O}_3$ at high Fe concentrations also depends on the preparation method and reaction conditions during experiments. Azimi et al. [43] prepared mixed oxides from powder mixtures of α - Mn_3O_4 and α - Fe_2O_3 via a spray drying method while Bhavsar et al. [17] prepared the mixed oxide by depositing Fe and Mn on the support material (CeO_2) with an incipient wetness technique. Both studies show that a bixbyite structure exists at Fe concentrations up to 90 % and the hematite phase appears beside the bixbyite phase. For Fe concentrations higher than 90%, only a hematite phase was found. Larring et al. [18] explored mixed oxides prepared from pure oxides, which were heated at temperatures equivalent to CL conditions under different oxygen pressures. Their analysis indicates that at Fe concentration of 87 %, 14% of a mixture has a bixbyite phase. Moreover, they found that the bixbyite phase can be found even at Fe concentration of 98 % depending on oxygen pressure. In the present study, we consider pure α - Mn_2O_3 and b - Fe_2O_3 as well as bixbyite $\text{Fe}_x\text{Mn}_{2-x}\text{O}_3$ at dopant concentrations of 3-50%, 75%, and 97%.

The optimized lattice parameter for α - Mn_2O_3 is 9.61 Å obtained by employing the same method as in the previous study [37]. The computed value is slightly larger than the experimental one [39] (difference of less than 2%) but agrees nicely with the previously computed lattice parameter [27]. Since the experimental lattice parameters of α - Mn_2O_3 and b - Fe_2O_3 are very close to each other (see Table 1), we used the optimized lattice parameter of α - Mn_2O_3 in all our calculations.

Fe atoms were considered as substitutional cation dopants in an α - Mn_2O_3 bixbyite structure. We gradually incorporated an increasing number of Fe atoms into the Mn sites of the α - Mn_2O_3 lattice and optimized atomic positions. For each dopant concentration, there are many ways to place dopants into the lattice and we carefully screened different distributions at each concentration and selected the one with the lowest energy for further studies. The full screening procedure is described in Section 2 of Supplementary material. The

representative set of structures, used in the study, is given in Figure 2. The calculations show that the first 8 Fe atoms (up to 25 % of Fe) prefer to substitute Mn atoms at the Wyckoff positions A leading to a very symmetrical and ordered structure. The remaining 24 Fe atoms fill Wyckoff positions D. This breaks down the symmetry and ordering of dopants, which is restored again at Fe concentration of 75 %.

Table 1. The comparison of calculated and experimental lattice parameters.

	Used in this study	Calculated Reference	Experimental reference
pure α - Mn_2O_3	9.61[37]	9.59 [27]	9.42 [39]
pure β - Fe_2O_3	9.61	—	9.40 [45]

Magnetic ordering in α - Mn_2O_3 is complex and has not been fully resolved [28,40]. A non-collinear antiferromagnetic (AFM) ordering model was first proposed by Grant et al. [46] but later studies showed that it does not explain the experimental data. Regulski et al. [40] proposed a model of collinear orientation of magnetic moments and demonstrated that it fits to neutron powder diffraction data. This AFM model is used in the present study to calculate band gaps for pure oxides. On the other hand, the previous calculations [27,37] have shown that α - Mn_2O_3 can be modeled as a ferromagnetic (FM) structure with the Mn atoms in a high-spin state configuration, because this approach introduces only a minor energy difference compared to the antiferromagnetic structure. Our calculations show, that oxygen vacancy formation energies in bulk α - Mn_2O_3 are very similar for both FM and AFM ordering being 2.2 and 2.3 eV respectively. We employ the FM ordering throughout the present study. According to experimental data [47], the magnetic ordering of pure β - Fe_2O_3 is also antiferromagnetic. Since we consider Fe atoms as substitutional defects in α - Mn_2O_3 , the magnetic structures of all Fe-doped Mn_2O_3 as well as pure β - Fe_2O_3 were taken to be ferromagnetic, where both Mn and Fe atoms are in their high-spin states.

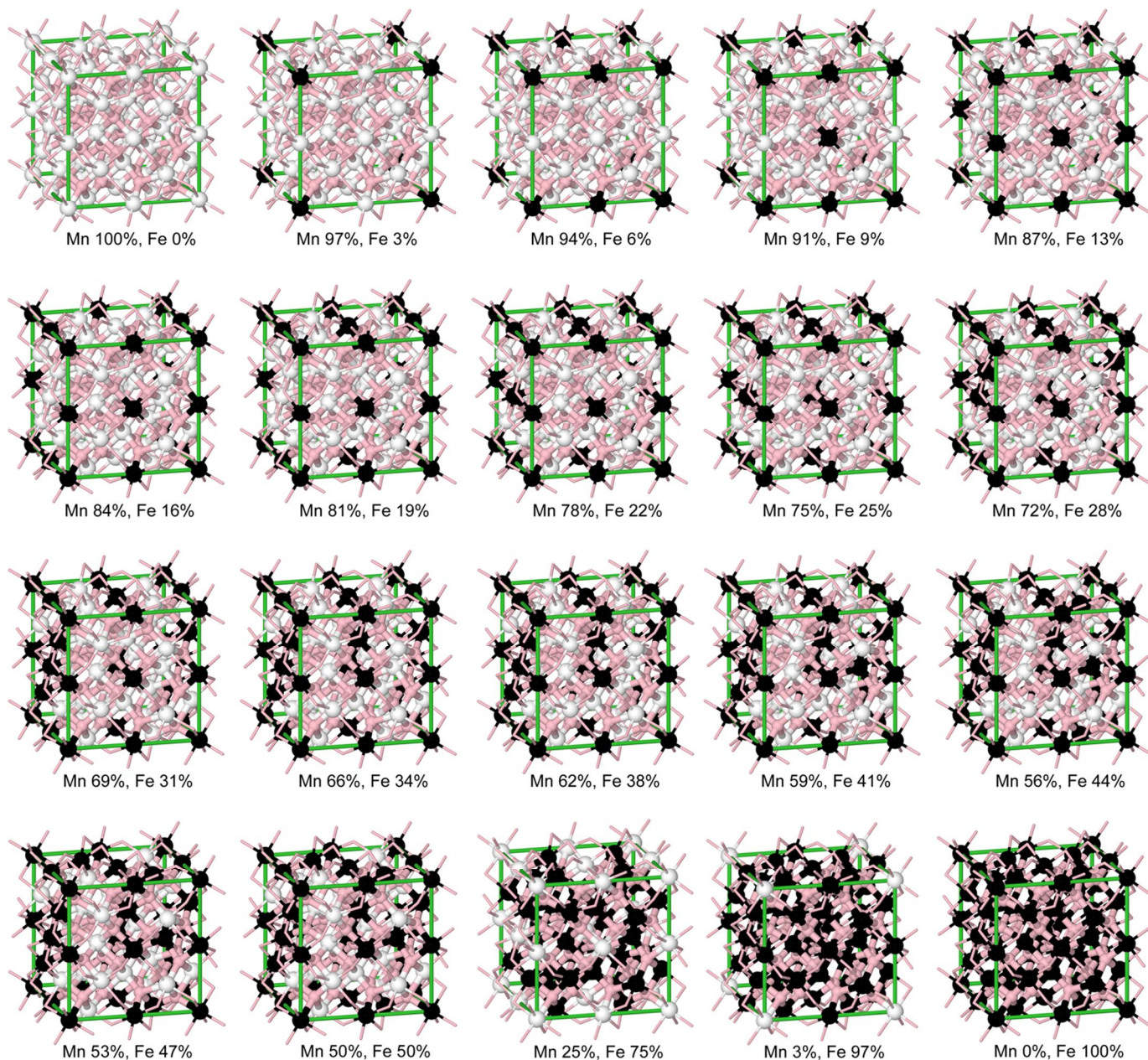


Figure 2. Different structure models for mixed oxides used in the current study. The notation below each structure indicates the content of Mn and Fe atoms, which was calculated as (the number of Mn atoms in the structure)*100/(the sum of Mn and Fe atoms in the structure). Mn atoms are shown in white, while Fe atoms are in black, and O atoms are in pink.

3. Results and discussion

3.1. Bulk properties of stoichiometric mixed oxides

According to experiments [39], replacing Mn cations with Fe cations in a bixbyite structure of α - Mn_2O_3 can stabilize the structure and prevent the formation of spinel γ - Mn_2O_3 . Computationally, the stabilization effect can be addressed by determining doping and oxide formation energies. Doping energies were computed to check how Fe dopants affect the stability of the oxide, and to estimate the favorability of a particular structure at given Fe concentration. Doping energy [48] was calculated as follows:

$$\Delta E_d = \frac{E_{mixoxide} - E_{Mn_2O_3} - xE_{FeO} + xE_{MnO}}{x}, \quad (1)$$

where $E_{mixoxide}$, $E_{Mn_2O_3}$, E_{FeO} , E_{MnO} are the total energies per a formula unit of a given oxide, and x is the doping ratio ($Fe_xMn_{2-x}O_3$) determined as follow:

$$x = \frac{2 \cdot Fe\%}{100}, \quad (2)$$

where $Fe\%$ is the iron content in the oxide.

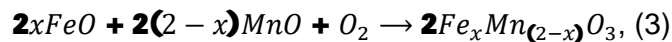
In the case of $Fe_xMn_{2-x}O_3$, all doping energies are negative, indicating doping to be favorable at studied Fe concentrations and energies range from -1.09 to -1.14 eV. The doping energy decreases from 0 to 25% Fe concentration and then increases for higher Fe concentrations. This fact can be explained by the symmetry and ordering of dopants. Eventually, the disturbance introduced by Fe dopants into the lattice can force the mixed oxide to obtain another crystallographic form [12,14,15,43,44]. This phase transition is a complex process and its explorations lies beyond the scope of this paper.

Next, we consider the structural properties of mixed oxide in more detail. Dopants may modify bond lengths in oxide, which can impact the reactivity of material [49]. Table 2 presents Me-O distances for doped oxide and gives the comparison between the calculated and experimental values. The computed bond lengths support the statement that metal atoms in different Wyckoff positions have different symmetry operations: we find that Me-O distances are equal for metal atoms located in Wyckoff position A, while the Me-O distance for metal atoms at Wyckoff position D varies up to 7%. In general, calculated Me-O distances agree well with experimental data: The replacement of a Mn cation with a Fe cation increases a Me-O distance for atoms located at the Wyckoff position A, and decreases the distance for metal atoms in the Wyckoff position D, in line with experimental evidence [39]. According to our calculations, Fe-O distances are slightly shorter than Mn-O distances, which indicates that the Fe-O bond is stronger than the Mn-O bond.

Table 2. The average metal-oxygen distance (in Å) and its standard deviations in the studied a- Mn_2O_3 , b- Fe_2O_3 , and $Fe_xMn_{2-x}O_3$.

Iron content, %	Metal atom at Wyckoff position A			Metal atom at Wyckoff position D		
	Mn—O, Å	Fe—O, Å	Experimental data [39] (Mn, Fe)—O, Å	Mn—O, Å	Fe—O, Å	Experimental data [39] (Mn, Fe)—O, Å
0	2.047±0.050	—	2.002±0.000	2.081±0.128	—	2.043±0.146
3	2.046±0.051	2.036±0.006	—	2.082±0.129	—	—
9	2.047±0.054	2.035±0.005	2.003±0.000	2.083±0.133	—	2.042±0.146
25	—	2.036±0.002	—	2.086±0.145	—	—
31	—	2.038±0.011	2.009±0.000	2.088±0.146	2.064±0.060	2.037±0.089
50	—	2.044±0.021	—	2.090±0.149	2.068±0.054	—
97	2.085±0.085	2.065±0.007	—	—	2.073±0.036	—
100	—	2.066±0.002	—	—	2.074±0.035	—

The bond strength can be estimated by determining oxide formation enthalpies (ΔH_f) [50], which were determined as follows:



$$\Delta H_f = E_{mixoxide} - (xE_{FeO} + (2-x)E_{MnO}) - \frac{1}{2}\mu_{O_2}, \quad (4)$$

where $E_{mixoxide}$, E_{FeO} , and E_{MnO} are total energies per formula unit for $Fe_xMn_{2-x}O_3$, FeO and MnO, respectively. The chemical potential of oxygen was computed at $T=0K$ and $p=0atm$, standard conditions ($T=298.15K$, $p=1atm$), and CLC conditions ($T=1200K$, $p=10^{-9}atm$). Since GGA calculations typically underestimate oxidation energies, Wang et.al. [36] proposed an energy correction of 1.36 eV, which is an energy difference between computed and measured oxidation energies of different transition metal oxides. This shift is suggested to be due to the fact that calculations underestimate O2 binding energy and the cost of adding an electron to the p orbital upon O_2^- formation [36]. Herein, we have corrected all the oxide formation energies by shifting the energies calculated according to equation 4 by 1.36 eV. This means that all the ΔH_f values plotted in Figure 3 are shifted upward by this constant, which does not impact the trends. In agreement with the previously computed value [36] and experimental data (-4.0 eV) [36], we obtained -3.95 eV (0K) for formation enthalpy of a- Mn_2O_3 . Replacing Mn cations with Fe cations increases oxide formation energies linearly (Figure 3) reaching the maximum value of -5.4 eV for pure b- Fe_2O_3 . This indicates that the strength of the Me-O bond increases with increasing Fe concentration, which on the other hand indicates more difficult oxygen removal compared to pure a- Mn_2O_3 . At higher temperature, ΔH_f becomes less negative indicating easier vacancy formation.

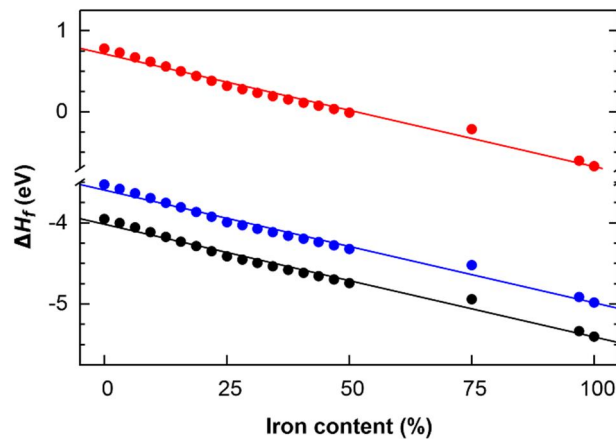


Figure 3. The oxide formation energy (ΔH_f) plotted as a function of Fe concentration in $Fe_xMn_{2-x}O_3$. Black color corresponds to ΔE at $T=0 K$ and $p=0 atm$, blue stands for normal conditions ($T=298.15 K$ and $p=1 atm$) and red is CLC conditions ($T=1200 K$, $p=10^{-9} atm$). For all trend lines $R^2=97.8\%$.

The formation of stronger Me-O bond in the presence of Fe and its impact on the reducibility of the material can be understood by analyzing the electronic and magnetic structure carefully. Figure 4 shows the evolution of the local density of state (LDOS) for $Fe_xMn_{2-x}O_3$ as a function of Fe concentration. We can see that replacing Mn with Fe gradually transforms half metal a- Mn_2O_3 into insulating b- Fe_2O_3 . The majority spin channel of a- Mn_2O_3 is metallic while the minority spin channel is insulating with the band gap of 4.8 eV in agreement with the previous DFT+U calculations [27]. The valence band edges of spin channels shift to different directions upon increasing the Fe content: the majority spin valence band edge shifts away from the Fermi level, while the minority-spin band edge moves toward the Fermi level. This behavior is independent of the Hubbard correction applied to Fe and Mn d electrons (Figure X in Supplementary material) because valence band edges for both spin channels are formed from oxygen p-orbitals and manganese d-orbitals but the shift of Mn

states is insignificant. Both spin channels are insulating for b-Fe₂O₃ and the band gap of for majority spin channel is 3.5 eV and 1.89 eV for the minority spin channel. Note that the lowest unoccupied state in majority spin channel is formed from oxygen p-orbitals and is delocalized over all oxygen atoms. Our calculations show that this state plays an important role in the formation of an oxygen vacancy that is discussed in Section 3.2. Table 3 summarizes the calculated and measured band gaps for a-Mn₂O₃ to b-Fe₂O₃. Band gaps computed herein for FM ordering compare reasonably well with previously reported values [27]. The comparison of computed band gaps to the measured ones is challenging. First, the experimental data corresponds to the antiferromagnetic ordering of an oxide. Second, the comparison of calculated AFM band gaps to the measured ones is hampered by the fact that the magnetic structure is incompletely resolved from experiments. Thus it is unclear how well the AFM model we employ corresponds to the real magnetic structure of the material for example in the case of α -Mn₂O₃.

The gradual change of band gaps as a function of Fe concentration is given in Figure 5. We note that, replacing one Fe in b-Fe₂O₃ with Mn (that corresponds to 97% of iron content) leads already to a large shift in a majority spin valence band edge toward the Fermi level. The careful analysis of Kohn-Sham wave functions unravel that the lowest unoccupied state in the major spin channel is an antibonding orbital formed from the d orbital of Mn and the p orbital of O. This also affects vacancy formation energy as discussed in Section 3.2.

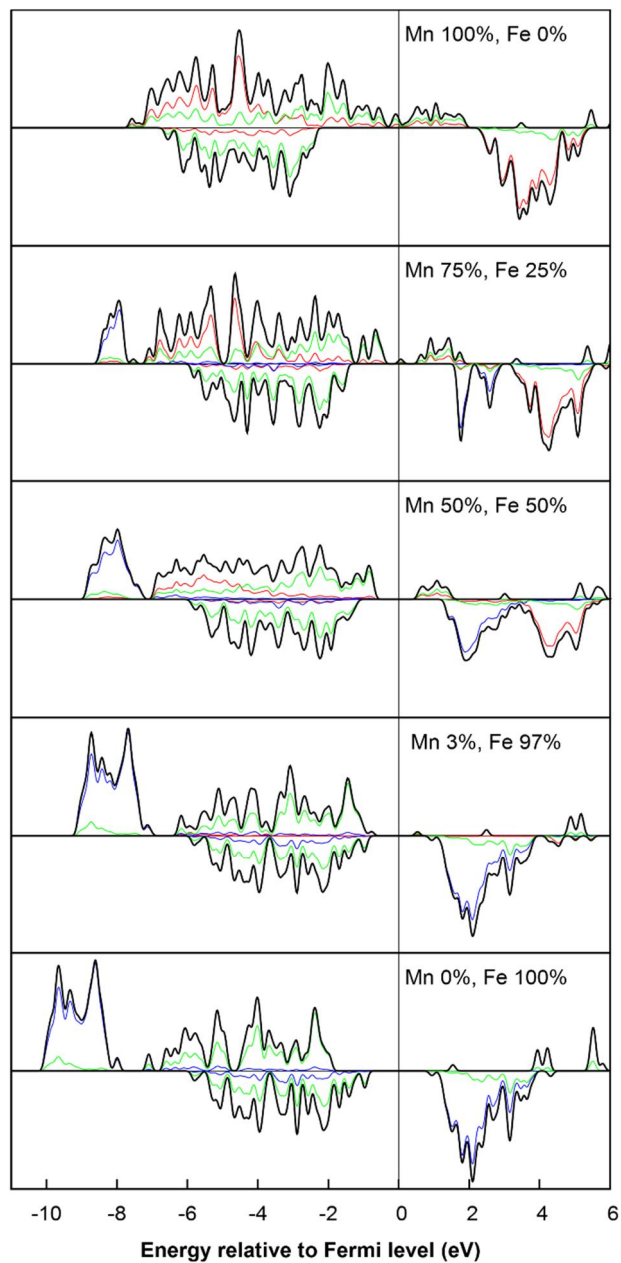


Figure 4. The local density of states for $\text{Fe}_x\text{Mn}_{2-x}\text{O}_3$. The black lines represent the total DOS, red lines give the LDOS of Mn d-electrons, blue lines stand for the LDOS of Fe d-electrons, and green lines the LDOS of O p-orbitals. The majority spin channel is shown upwards and the minority spin channel is given downwards.

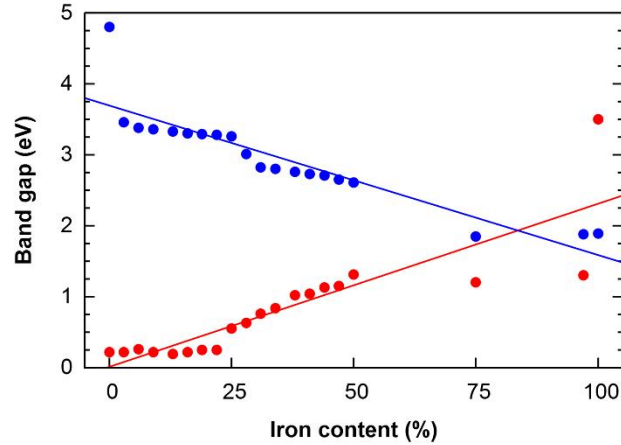


Figure 5. The band gap of $\text{Fe}_x\text{Mn}_{2-x}\text{O}_3$ as a function of Fe concentration. Red dots corresponds to the major spin channel and blue dots stand for the minor spin channel. The solid lines are to guide the eye.

Table 3. The comparison of calculated and experimentally obtained band gaps for pure a- Mn_2O_3 and b- Fe_2O_3 (HM – half-metallic). Experimental data is presented for an antiferromagnetic structure, while the computed data corresponds to ferromagnetic ordering.

Oxide	Computational value (FM ordering) (spin-up/spin-down DOS)	Computational reference value (FM ordering)	Computational value (AFM ordering)	Experimental value (AFM ordering)
a- Mn_2O_3	0.2/4.8	HM/3.5 [27]	0.9/0.9	1.9-2.1 [51]
b- Fe_2O_3	3.5/1.90	—	2.1/2.1	2.2 [47]

Table 4 summarizes computed magnetic moments and compares them to measured magnetic moments. The average magnetic moments of Mn and Fe atoms are $4.1\mu_0$ and $4.5\mu_0$, respectively. The Bader charge analysis [52], also given in Table 4, presents the average charges $+1.8e$ and $+1.9e$ for Mn and Fe cations, respectively (formal oxidation state of $+3$), and $-1.2e$ for oxygen (formal oxidation state -2). The smaller oxidation state compared to the formal oxidation state is tentatively ascribed to the partial covalent nature of the metal-oxygen bond.

Table 4. Local magnetic moments and Bader charges.

Oxide	Magnetic moments on Mn/Fe atoms, μ_0			Bader Charges on Mn/Fe/O atoms	
	Calc.	Calc. ref.	Exp.	Calc.	Formal oxidation state
α - Mn_2O_3	4.1/—	3.6[28]/—	(AFM 3.8 ± 0.2 [40])	+1.8/—/-1.2	+3.0/—/+2
$\text{Fe}_x\text{Mn}_{2-x}\text{O}_3$	4.1/4.4	—	—	+1.8/+1.9/-1.2	+3.0/+3.0/+2
β - Fe_2O_3	—/4.5	—	—	—/+1.9/-1.2	—/+3.0/+2

3.2. Formation of single oxygen vacancy

Efficient release of oxygen is one of the key properties of promising CL carrier materials and it begins with the removal of the first oxygen and the formation of an oxygen vacancy. Herein, we are specifically interested in how Fe cations impact on the vacancy formation

energy and thus the ability of the material to release oxygen. In general, the oxygen vacancy formation energy gives valuable information about the thermal stability of the material. We considered one oxygen vacancy per a unit cell for all possible different oxygen positions in $\text{Fe}_x\text{Mn}_{2-x}\text{O}_3$. In the case Fe content is below 25%, two inequivalent sites for oxygen vacancies exist: site A with only neighboring Mn atoms, and site B with 1 Fe and 3 Mn neighbors. At higher Fe concentration ranging from >25% to 75 %, oxygen vacancy sites are always surrounded by both Fe and Mn atoms and three inequivalent sites are possible: site B, site C with 2 Fe and 2 Mn neighbors, and site D with 3 Fe and 1 Mn neighbors. For very high iron concentrations (>75%) vacancy sites can be either D-site, or site E with 4 adjacent Fe atoms.

For each case, the vacancy formation energy (ΔE), that is calculated as follows:

$$\Delta E = E_V + \frac{1}{2}\mu_{O_2} - E_{mixoxide} - k_b T \ln \frac{N!}{n!(N-n)!}, \quad (5)$$

where E_V and $E_{mixoxide}$ are total energies for reduced (one missing oxygen) and stoichiometric oxide, respectively, and μ_{O_2} is the chemical potential for gas-phase oxygen. The last term is the configurational entropy, in which n is the number of vacancies in the unit cell and N is the number of equivalent vacancy sites. The results are reported in Figure 6, which presents vacancy formation energy as a function of Fe concentration for different vacancy sites under $T= 0\text{K}$, normal conditions, and typical CL conditions. For comparison, we give the vacancy formation energies for pure oxides as well, which show that the vacancy formation energy for b- Fe_2O_3 is substantially larger than for a- Mn_2O_3 . Thus, it is not surprising that increase in Fe concentration leads to higher vacancy formation energies. Figure 6 shows that vacancy formation energy for site A is slightly smaller than for site B, which, on the other hand, is slightly more favorable than for sites C and D. Under CL conditions, vacancy formation at site A is spontaneous because vacation formation energy is negative, while it is thermoneutral for site B. Our calculations show that the formation of the second oxygen vacancy in a- Mn_2O_3 is equally favorable to the formation of the first oxygen vacancy. Spontaneous reducibility of $\alpha\text{-Mn}_2\text{O}_3$ has implications for reactivity of as oxygen defects are typical active sites for many reactions. Furthermore, we note that at Fe concentration of 97 %, the presence of even one Mn cation improves the reducibility of $\beta\text{-Fe}_2\text{O}_3$ compared to pure b- Fe_2O_3 . In general, the energy variation as a function of Fe concentration seen in Figure 6 supports the prediction based on experimental data [18].

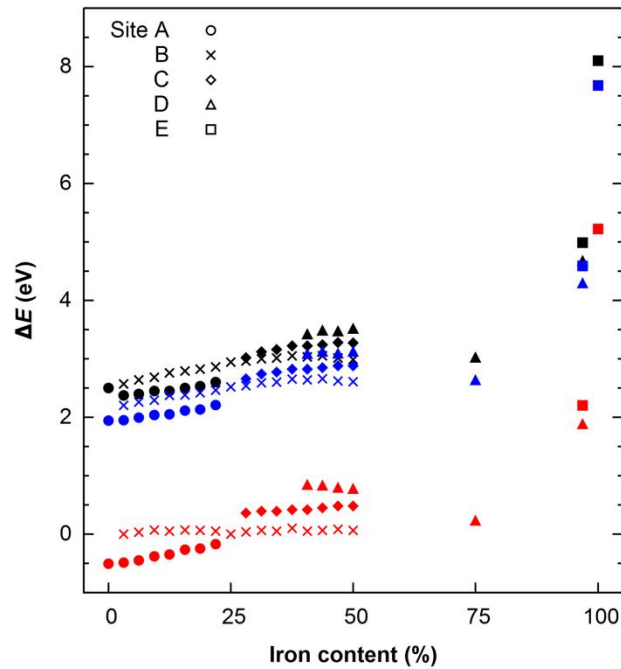


Figure 6. The effect of concentration onto the vacancy formation energy in $\text{Fe}_x\text{Mn}_{2-x}\text{O}_3$ oxide. Data points represent average values of the vacancy formation energies. Black color corresponds to ΔE at $T=0\text{K}$, blue – to normal conditions ($T=298.15\text{K}$ and $p=1\text{atm}$), red – to CLC conditions ($T=1200\text{K}$, $p=10^{-9}\text{atm}$). Shapes of dots represent types of vacancies, for example, notation “Site A” means that vacancy is adjacent to 4Mn and 0 Fe atoms.

Higher vacancy formation energies for Fe-rich oxide can be linked to a stronger Fe-O bond indicated also by more exothermic formation energy of the oxide. Computed vacancy formation energies nicely support the experimental findings that Fe dopants improve the thermodynamic stability of Mn-based oxide [43].

On the other hand, we note that in general the changes in vacancy formation energy are linked to the changes in band gap values in the majority spin channel: the large decrease in the band gap of the majority spin channel is seen when one Fe cation is replaced with a Mn cation in $\text{b-Fe}_2\text{O}_3$. This leads to a significant drop in vacancy formation energy as seen from Figure 3 in Supplementary material, while small changes in band gap values for oxides with 0-50% of Fe introduce to small changes in vacancy formation energy. This behavior is tentatively ascribed to higher electron affinity of Mn, which is in line with the changes in Bader charges displayed in Figure 7. We found that upon the formation of an oxygen vacancy, excessive electrons localize on the nearest metal cations. While the distribution of electrons between four nearest cations in the pure oxide is homogeneous, the situation changes in the presence of Fe dopants and electron localization favors Mn cations in $\text{Fe}_x\text{Mn}_{2-x}\text{O}_3$. Moreover, the effect becomes more enhanced with increasing Fe concentration, and is the most pronounced in $\text{Fe}_x\text{Mn}_{2-x}\text{O}_3$ with one Mn cation.

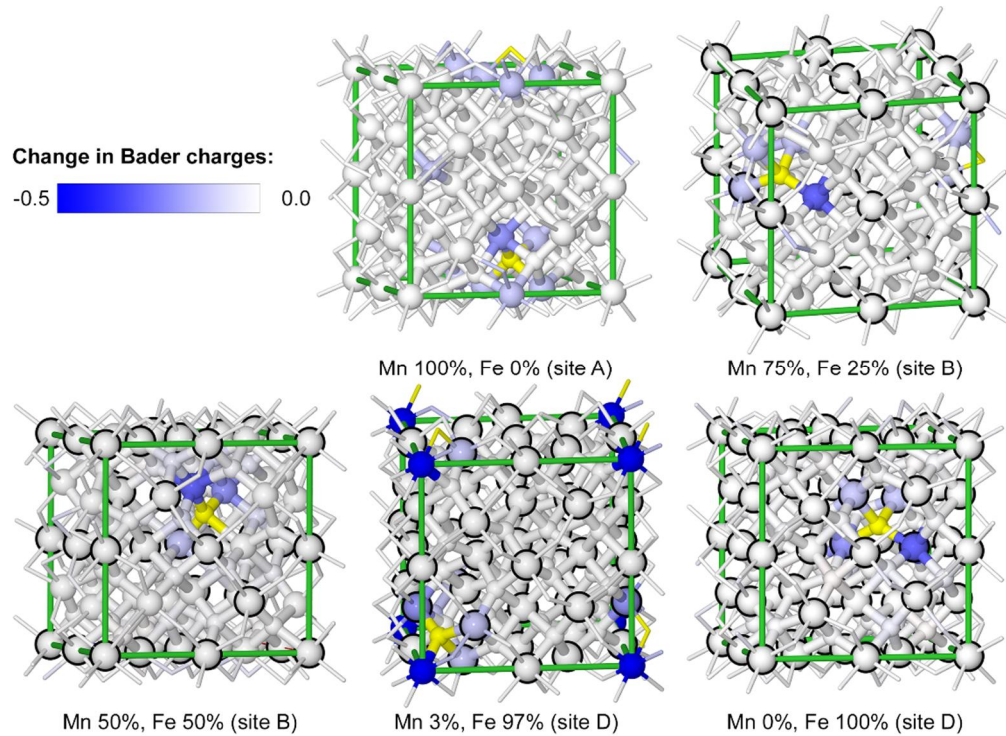


Figure 7. The distribution of excessive electrons left after vacancy formation. Yellow color represents the position of an oxygen vacancy, iron atoms are denoted with the black rim, the blue gradient indicates changes in Bader charges on atoms.

Changes in electronic structure introduced by an oxygen vacancy are minor for Mn rich materials whereas significant changes are seen for Fe-rich oxides as shown in LDOS plots in Figure 8. The variation of band gaps for oxygen deficient material is similar to stoichiometric oxide: the band gap of the majority-spin channel increases, while the band gap of the minority spin channel decreases with increasing of iron content. The analysis of the electronic structure and Kohn-Sham single particle wave functions shows that the large shift in the electronic structure seen for the majority spin in 3% Mn- and pure Fe_2O_3 is due to the occupation of one O 2p -derived state in an oxygen deficient system, which is empty in stoichiometric oxide.

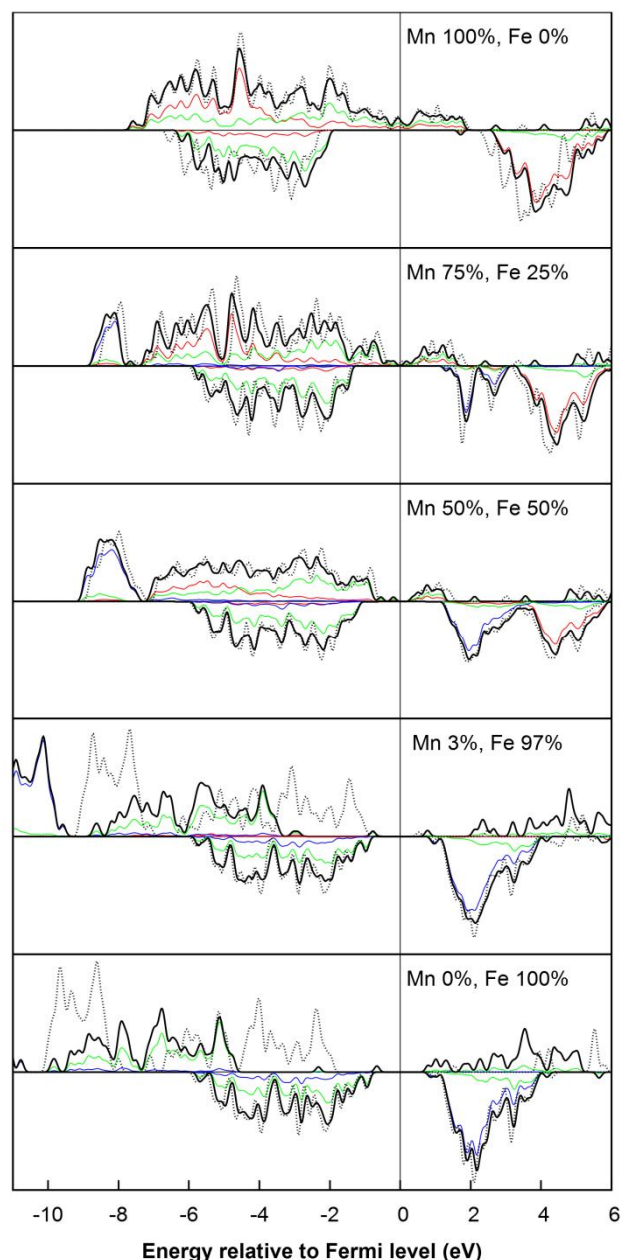


Figure 8. The Electronic density of states for mixed oxides with an oxygen vacancy. Solid lines corresponds to oxides with vacancy: black lines represent total DOS, red lines stand for the DOS of Mn d electrons, blue lines are the DOS of Fe d electrons, green lines while the DOS of O p electrons. The dotted gray line shows the total DOS for particular stoichiometric oxide. Majority and minority states are shown as positive and negative curves. The studied vacancy sites (from top to down) are following A (Mn 100%), B (Mn 75 %, Fe 25%), B (Mn 50%, Fe 50%), D (Mn 3%, 97%), and (Mn 0%, Fe 100%).

The formation of an oxygen vacancy disturbs an oxide lattice and introduces changes in the positions of cations, adjacent to the vacancy. We analyzed changes in metal-oxygen distances for all the studied structures, and obtained results are summarized in Table 5. In general, we find that the cations move away from the vacancy and this is more pronounced for Fe than for Mn cations.

Table 5. The average changes and standard deviations in distances between metal atoms, adjacent to a vacancy, to a position, where the oxygen atom used be before vacancy formation.

Oxide	Type of atoms adjacent to oxygen vacancy	Change in distance (Å) between a metal cation and a site with O/vacancy	
		Mn—vac	Fe—vac
a-Mn ₂ O ₃	A site	0.12±0.03	—
Fe _x Mn _{2-x} O ₃ , 3% Fe	A site	0.13±0.04	—
	B site	0.20±0.02	0.00
Fe _x Mn _{2-x} O ₃ , 25% Fe	B site	0.13±0.02	0.23
Fe _x Mn _{2-x} O ₃ , 50% Fe	B site	0.11±0.02	0.23
	C site	0.11±0.04	0.24±0.01
	D site	0.09	0.27±0.04
b-Fe ₂ O ₃	E site	—	0.10±0.02

3.3. Oxygen diffusion

The migration of oxygen was studied for Fe_xMn_{2-x}O₃ containing 0%, 25%, 50%, 100% of Fe, where two pathways are possible for oxygen diffusion namely edge and facet paths, shown in Figure 9. Oxygen atoms in Fe_xMn_{2-x}O₃ lie in the middle of tetrahedrons, formed by four neighboring metal cations.

The edge path (EP) corresponds to the diffusion of oxygen through the edges of two connecting tetrahedrons, and represents oxygen transport to the nearest oxygen position. The facet path (FP) goes through the facet of tetrahedrons and corresponds to oxygen diffusion to the next nearest position. Figure 9 also shows the transition state geometries for both pathways. While in the EP, the transition state is between two cations along a line, the transition state of the FP is more complex and includes several metal cations.

Table 6 summarizes the average computed diffusion barriers for both EP and FP in different oxides. In general, we find that the activation barriers for EP channels are lower than for the FP channels. As seen from the standard deviation values given in Table 6, the barrier heights vary for mixed oxides. These variations originate from differences in a chemical composition of initial, transition and final states.

For pure a-Mn₂O₃ and b-Fe₂O₃ all the oxygen anions are equivalent and the chemical compositions of initial, final and transitions states remain similar no matter which oxygen atom is moving. This leads to only very minor deviations in diffusion barriers along both pathways. However, in mixed oxides Mn and Fe atoms can be distributed unevenly in the computational cell, which introduces significant variation to a diffusion barrier, which sensitively depends on the particular distribution of Mn and Fe atoms. We carefully studied and analyzed different diffusion paths for mixed oxide containing 25% and 50% of Fe and observed that the variation of a diffusion barrier is extremely complex phenomenon and general trends are difficult to find due to the fact that the barrier height depends on multiple parameters as highlighted below.

To start with, the symmetrical mixed oxide with 25% of Fe is discussed. In this case, the transition state of EP can form either from two Mn atoms at the edge, or from one Mn and one Fe atom at the edge. The transition state having only Mn atoms leads to a lower diffusion barrier (0.90 eV in average) compared to the transition state of both Mn and Fe atoms (1.16 eV in average). The transition state along the FP can have several different chemical compositions and distributions, where the lowest barrier corresponds to the

transition state with 4 Mn atoms in the base of a pyramid (shown in Figure 9) and a Fe atom at the apex, while the highest barrier is found for the transition states with 5 Mn atoms.

Mixed oxide with 50 % of Fe demonstrates a very anisotropic structure, which in this case means that the distribution of Fe cations is non-homogeneous. We find that anisotropy introduces large variations in chemical surroundings and barrier heights and therefore, the comparison of different transition state energies along (EP or FP) becomes challenging. One potential additional factor contributing to the barrier height can be chemical composition surrounding the diffusing oxygen at the initial state. We computed 22 edge paths and 40 facet paths with different TS and initial structures. In the case of EP, there are 3 possible combinations (Mn-Mn, Fe-Mn and Fe-Fe) of metal atoms that can constitute the transition state, while for FP we already found 8 possible combinations of cations for the transition state. Both paths can have three different initial structures (3Mn and 1Fe atoms adjacent to diffusing oxygen, 2Mn and 2Fe, and 3Fe and 1Mn). The majority of computed activation barriers range from 0.7 to 1.1 eV for the EP and from 0.7 to 1.8 eV for the FP. Due to the large number of different initial state – transition state combinations, the origin of activation energy variation is challenging to pinpoint. Furthermore, we noticed that the chemical nature of the next nearest metal atoms also has an impact on the barrier height. Therefore, it is hardly surprising that the variation of an activation barrier for mixed oxide with Fe concentration of 50% is even more complex and its rationalization calls for descriptors for long range structural effects. These long range effects can potentially originate from variations in Fe concentration along a diffusion pathway.

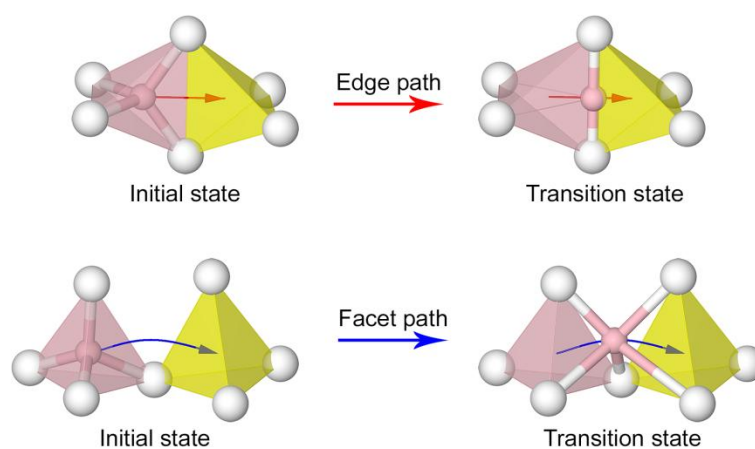


Figure 9. The schematic representation of edge and facet diffusion paths. Metal atoms are shown in white and the oxygen atom is given in pink. The pink tetrahedron corresponds to the initial position of an oxygen atom and the yellow tetrahedron stands for the position of an oxygen vacancy. The arrow represents the diffusion path, where the end of an arrow shows the initial and final position of an oxygen atom. The red (blue) arrow describes the edge (facet) path.

Table 6. The average diffusion barrier heights for Mn_2O_3 and $\text{Fe}_x\text{Mn}_{2-x}\text{O}_3$. The second number gives the standard deviation for a barrier. Activation barriers for pure $\alpha\text{-Mn}_2\text{O}_3$ are taken from Ref.[37].

Oxide	Edge path	Facet path
$\alpha\text{-Mn}_2\text{O}_3$	0.7 [37]	1.0 [37]
$\text{Fe}_x\text{Mn}_{2-x}\text{O}_3$, 25% Fe	1.0 ± 0.1	1.2 ± 0.2
$\text{Fe}_x\text{Mn}_{2-x}\text{O}_3$, 50% Fe	0.9 ± 0.2	1.3 ± 0.5
$\beta\text{-Fe}_2\text{O}_3$	1.4 ± 0.0	1.7 ± 0.1

CONCLUSION

This work provides a systematic study on bulk properties, vacancy formation and oxygen diffusion in Fe doped Mn_2O_3 . Using DFT calculations employing the GGA+U approach several thousand structures were carefully screened as a function of Fe concentration and distribution. A representative set of 20 structures at the range of 0-50%, 75%, 97%, and 100% Fe concentration was selected for a more careful analysis.

Our calculations indicate that substitution of Mn cations with Fe cations in $\alpha\text{-Mn}_2\text{O}_3$ improves the stability of the oxide, which is reflected in negative values of doping energies and more exothermic oxide formation energies with increasing of iron concentration. This is due to the fact that the Fe-O bond is stronger than the Mn-O bond. The presence of Fe dopants also changes the electronic structure of the oxide: the majority spin channel transforms from half-metallic to clearly insulating with a non-zero band gap while the band gap of minority spin channel slowly decreases with increasing Fe concentration.

Formation of an oxygen vacancy was examined for each structure in the representative set. Our findings support the conclusion that introduction of Fe atoms stabilizes the Mn_2O_3 because the vacancy formation energy increases with the increasing number of Fe dopants in the lattice. Excess electrons left to oxide upon oxygen removal modify electronic and magnetic properties of the oxide. Specifically, excess electrons distribute on the nearest neighbor cations, primarily to Mn. The changes in the local density of states are mainly seen for major spin channel at high Fe concentration.

Oxygen transport studies highlight the rich variation of diffusion barrier values depending on Fe concentration and distribution, in particular this is visible at Fe concentration above 50%. In general, the diffusion pathway via the transition state located between two cations, the so-called edge pathway is kinetically more favorable than the facet pathway, which is another possible migration channel. The Fe dopants hinder oxygen migration but even for pure $\beta\text{-Fe}_2\text{O}_3$ the diffusion barrier for the edge pathway is only 1.4 eV, which hardly can dominate the performance of material in CL applications.

Overall, our study presents atomic-level explanation for experimentally observed stabilization and improved performance of Fe-doped Mn_2O_3 in CL applications. The systematic screening approach employed herein to study bulk properties of $\text{Fe}_x\text{Mn}_{2-x}\text{O}_3$ oxide can be readily extendible to examine reactivity of the oxides towards oxidation of fuels.

ACKNOWLEDGEMENTS

We gratefully acknowledge the financial support from the Fortum Foundation (B2-scholarship: 201500030, 201600030). Electronic structure calculations were made possible through the use of computational resources provided by CSC - IT Center for Science in Espoo, Finland. We also thank MSc. Minttu Kauppinen for careful reading of the paper and Dr. Andrey Bazhenov for fruitful discussions.

REFERENCES

- [1] L.-S. Fan, L. Zeng, W. Wang, S. Luo, Chemical looping processes for CO₂ capture and carbonaceous fuel conversion – prospect and opportunity, *Energy Environ. Sci.* 5 (2012) 7254. doi:10.1039/c2ee03198a.
- [2] Q. Song, W. Liu, C.D. Bohn, R.N. Harper, E. Sivaniah, S. a. Scott, et al., A high performance oxygen storage material for chemical looping processes with CO₂

- capture, *Energy Environ. Sci.* 6 (2013) 288. doi:10.1039/c2ee22801g.
- [3] S. Bhavsar, M. Najera, R. Solunke, G. Vesper, Chemical looping: To combustion and beyond, *Catal. Today.* 228 (2014) 96–105. doi:10.1016/j.cattod.2013.12.025.
- [4] J. Adanez, A. Abad, F. Garcia-Labiano, P. Gayan, L.F. de Diego, Progress in Chemical-Looping Combustion and Reforming technologies, *Prog. Energy Combust. Sci.* 38 (2012) 215–282. doi:10.1016/j.peccs.2011.09.001.
- [5] A. Thursfield, A. Murugan, R. Franca, I.S. Metcalfe, Chemical looping and oxygen permeable ceramic membranes for hydrogen production – a review, *Energy Environ. Sci.* 5 (2012) 7421. doi:10.1039/c2ee03470k.
- [6] M.M. Hossain, H.I. de Lasa, Chemical-looping combustion (CLC) for inherent CO₂ separations—a review, *Chem. Eng. Sci.* 63 (2008) 4433–4451. doi:10.1016/j.ces.2008.05.028.
- [7] T. Mattisson, A. Lyngfelt, H. Leion, Chemical-looping with oxygen uncoupling for combustion of solid fuels, *Int. J. Greenh. Gas Control.* 3 (2009) 11–19. doi:10.1016/j.ijggc.2008.06.002.
- [8] A. Shulman, E. Cleverstam, T. Mattisson, A. Lyngfelt, Chemical – Looping with oxygen uncoupling using Mn/Mg-based oxygen carriers – Oxygen release and reactivity with methane, *Fuel.* 90 (2011) 941–950. doi:10.1016/j.fuel.2010.11.044.
- [9] M. Johansson, T. Mattisson, A. Lyngfelt, Creating a synergy effect by using mixed oxides of iron- and nickel oxides in the combustion of methane in a chemical-looping combustion reactor, *Energy and Fuels.* 20 (2006) 2399–2407. doi:10.1021/ef060068l.
- [10] M. Källén, P. Hallberg, M. Rydén, T. Mattisson, A. Lyngfelt, Combined oxides of iron, manganese and silica as oxygen carriers for chemical-looping combustion, *Fuel Process. Technol.* 124 (2014) 87–96. doi:10.1016/j.fuproc.2014.02.020.
- [11] D. Jing, M. Arjmand, T. Mattisson, M. Rydén, F. Snijkers, H. Leion, et al., Examination of oxygen uncoupling behaviour and reactivity towards methane for manganese silicate oxygen carriers in chemical-looping combustion, *Int. J. Greenh. Gas Control.* 29 (2014) 70–81. doi:10.1016/j.ijggc.2014.07.003.
- [12] A. Lambert, C. Delquié, I. Clémeneçon, E. Comte, V. Lefebvre, J. Rousseau, et al., Synthesis and characterization of bimetallic Fe/Mn oxides for chemical looping combustion, *Energy Procedia.* 1 (2009) 375–381. doi:10.1016/j.egypro.2009.01.051.
- [13] M. Rydén, A. Lyngfelt, T. Mattisson, Combined manganese/iron oxides as oxygen carrier for chemical looping combustion with oxygen uncoupling (CLOU) in a circulating fluidized bed reactor system, *Energy Procedia.* 4 (2011) 341–348. doi:10.1016/j.egypro.2011.01.060.
- [14] G. Azimi, H. Leion, T. Mattisson, A. Lyngfelt, Chemical-looping with oxygen uncoupling using combined Mn-Fe oxides, testing in batch fluidized bed, *Energy Procedia.* 4 (2011) 370–377. doi:10.1016/j.egypro.2011.01.064.
- [15] G. Azimi, H. Leion, M. Rydén, T. Mattisson, A. Lyngfelt, Investigation of Different Mn–Fe Oxides as Oxygen Carrier for Chemical-Looping with Oxygen Uncoupling (CLOU), *Energy & Fuels.* 27 (2013) 367–377. doi:10.1021/ef301120r.
- [16] A. Shulman, E. Cleverstam, T. Mattisson, A. Lyngfelt, Manganese/Iron, Manganese/Nickel, and Manganese/Silicon Oxides Used in Chemical-Looping With Oxygen Uncoupling (CLOU) for Combustion of Methane, *Energy & Fuels.* 23 (2009) 5269–5275. doi:10.1021/ef9005466.

- [17] S. Bhavsar, B. Tackett, G. Veser, Evaluation of iron- and manganese-based mono- and mixed-metallic oxygen carriers for chemical looping combustion, *Fuel*. 136 (2014) 268–279. doi:10.1016/j.fuel.2014.07.068.
- [18] Y. Larring, C. Braley, M. Pishahang, K.A. Andreassen, R. Bredesen, Evaluation of a Mixed Fe–Mn Oxide System for Chemical Looping Combustion, *Energy & Fuels*. 29 (2015) 3438–3445. doi:10.1021/acs.energyfuels.5b00048.
- [19] C. Dong, S. Sheng, W. Qin, Q. Lu, Y. Zhao, X. Wang, et al., Density functional theory study on activity of α -Fe₂O₃ in chemical-looping combustion system, *Appl. Surf. Sci.* 257 (2011) 8647–8652. doi:10.1016/j.apsusc.2011.05.042.
- [20] C. Lin, W. Qin, C. Dong, Reduction effect of α -Fe₂O₃ on carbon deposition and CO oxidation during chemical-looping combustion, *Chem. Eng. J.* 301 (2016) 257–265. doi:10.1016/j.cej.2016.04.136.
- [21] W. Qin, Q. Chen, Y. Wang, C. Dong, J. Zhang, W. Li, et al., Theoretical study of oxidation-reduction reaction of Fe₂O₃ supported on MgO during chemical looping combustion, *Appl. Surf. Sci.* 266 (2013) 350–354. doi:10.1016/j.apsusc.2012.12.023.
- [22] Q. Tan, W. Qin, Q. Chen, C. Dong, W. Li, Y. Yang, Synergetic effect of ZrO₂ on the oxidation–reduction reaction of Fe₂O₃ during chemical looping combustion, *Appl. Surf. Sci.* 258 (2012) 10022–10027. doi:10.1016/j.apsusc.2012.06.067.
- [23] C. Dong, X. Liu, W. Qin, Q. Lu, X. Wang, S. Shi, et al., Deep reduction behavior of iron oxide and its effect on direct CO oxidation, *Appl. Surf. Sci.* 258 (2012) 2562–2569. doi:10.1016/j.apsusc.2011.10.092.
- [24] W. Qin, Y. Wang, C. Dong, J. Zhang, Q. Chen, Y. Yang, The synergetic effect of metal oxide support on Fe₂O₃ for chemical looping combustion: A theoretical study, *Appl. Surf. Sci.* 282 (2013) 718–723. doi:10.1016/j.apsusc.2013.06.041.
- [25] M. Wang, J. Liu, F. Shen, H. Cheng, J. Dai, Y. Long, Theoretical study of stability and reaction mechanism of CuO supported on ZrO₂ during chemical looping combustion, *Appl. Surf. Sci.* 367 (2016) 485–492. doi:10.1016/j.apsusc.2016.01.240.
- [26] Z. Cheng, L. Qin, M. Guo, J.A. Fan, D. Xu, L.-S. Fan, Methane adsorption and dissociation on iron oxide oxygen carriers: the role of oxygen vacancies, *Phys. Chem. Chem. Phys.* 18 (2016) 16423–16435. doi:10.1039/C6CP01287F.
- [27] C. Franchini, R. Podloucky, J. Paier, M. Marsman, G. Kresse, Ground-state properties of multivalent manganese oxides: Density functional and hybrid density functional calculations, *Phys. Rev. B.* 75 (2007) 195128. doi:10.1103/PhysRevB.75.195128.
- [28] E. Cockayne, I. Levin, H. Wu, A. Llobet, Magnetic structure of bixbyite α -Mn₂O₃: A combined DFT+U and neutron diffraction study, *Phys. Rev. B.* 87 (2013) 184413. doi:10.1103/PhysRevB.87.184413.
- [29] H.-Y. Su, Y. Gorlin, I.C. Man, F. Calle-Vallejo, J.K. Nørskov, T.F. Jaramillo, et al., Identifying active surface phases for metal oxide electrocatalysts: a study of manganese oxide bi-functional catalysts for oxygen reduction and water oxidation catalysis, *Phys. Chem. Chem. Phys.* 14 (2012) 14010. doi:10.1039/c2cp40841d.
- [30] K.W. Mortensen, J. J.; Hansen, L. B.; Jacobsen, Real-space Grid Implementation of the Projector augmented Wave method, *Phys. Rev. B.* 71 (2005).
- [31] H.A. et al. Enkovaara, J.; Rostgaard, C.; Mortensen, J. J.; Chen, J.; Dułak, M.; Ferrighi, L.; Gavnholt, J.; Glinsvad, C.; Haikola, V.; Hansen, Electronic Structure Calculations with GPAW: a Real-Space Implementation of the Projector Augmented-wave Method, *J. Phys. Condens. Matter.* 22 (2010) 253202.

- [32] K.W. Bahn, S. R.; Jacobsen, An Object-oriented Scripting Interface to a Legacy Electronic Structure Code, *Comput. Sci. Eng.* 4 (2002) 56–66.
- [33] J. Perdew, K. Burke, M. Ernzerhof, Generalized Gradient Approximation Made Simple., *Phys. Rev. Lett.* 77 (1996) 3865–3868. doi:10.1103/PhysRevLett.77.3865.
- [34] V.I. Anisimov, J. Zaanen, O.K. Andersen, Band theory and Mott insulators: Hubbard U instead of Stoner I, *Phys. Rev. B.* 44 (1991) 943–954. doi:10.1103/PhysRevB.44.943.
- [35] M. Cococcioni, S. de Gironcoli, A linear response approach to the calculation of the effective interaction parameters in the LDA+U method, *Phys. Rev. B.* 71 (2004) 18. doi:10.1103/PhysRevB.71.035105.
- [36] L. Wang, T. Maxisch, G. Ceder, Oxidation energies of transition metal oxides within the GGA + U framework, *Phys. Rev. B.* 73 (2006) 195107. doi:10.1103/PhysRevB.73.195107.
- [37] T. Parviainen, Computational studies of Chemical Looping combustion materials and CO₂ activating surfaces, University of Jyväskylä, 2016.
- [38] H. Jonson, G. Mills, K.W. Jacobsen, Nudged elastic band method for finding minimum energy paths of transitions, in: *Class. Quantum Dyn. Condens. Phase Simulations*, 1998: pp. 385–404. doi:10.1142/9789812839664_0016.
- [39] S. Geller, Structure of α -Mn₂O₃, (Mn_{0.983}Fe_{0.017})₂O₃ and (Mn_{0.37}Fe_{0.63})₂O₃ and relation to magnetic ordering, *Acta Crystallogr. Sect. B Struct. Crystallogr. Cryst. Chem.* 27 (1971) 821–828. doi:10.1107/S0567740871002966.
- [40] M. Regulski, R. Przeniosło, I. Sosnowska, D. Hohlwein, R. Schneider, Neutron diffraction study of the magnetic structure of α -Mn₂O₃, *J. Alloys Compd.* 362 (2004) 236–240. doi:10.1016/S0925-8388(03)00591-7.
- [41] Bilbao crystallographic server, (n.d.). <http://www.cryst.ehu.es/>.
- [42] H. Wondratschek, Special topics on space groups, in: *Int. Tables Crystallogr.*, International Union of Crystallography, Chester, England, 2006: pp. 732–740. doi:10.1107/97809553602060000516.
- [43] G. Azimi, M. Rydén, H. Leion, T. Mattisson, A. Lyngfelt, (Mn_zFe_{1-z})₂O₃ combined oxides as oxygen carrier for chemical-looping with oxygen uncoupling, *AIChE J.* 59 (2013) 582–588. doi:10.1002/aic.13847.
- [44] S.N. de Medeiros, A. Luciano, L.F. Cótica, I.A. Santos, A. Paesano, J.B.M. da Cunha, Structural and magnetic characterization of the ball-milled α -Fe₂O₃–Mn₂O₃ and α -Fe–Mn₂O₃ systems, *J. Magn. Mater.* 281 (2004) 227–233. doi:10.1016/j.jmmm.2004.04.109.
- [45] T. Danno, D. Nakatsuka, Y. Kusano, H. Asaoka, M. Nakanishi, T. Fujii, et al., Crystal Structure of β -Fe₂O₃ and Topotactic Phase Transformation to α -Fe₂O₃, *Cryst. Growth Des.* 13 (2013) 770–774. doi:10.1021/cg301493a.
- [46] R.W. Grant, S. Geller, J.A. Cape, G.P. Espinosa, Magnetic and Crystallographic Transitions in the α - α' -Mn₂O₃, *Phys. Rev.* 175 (1968) 686–695. doi:10.1103/PhysRev.175.686.
- [47] O. Malina, J. Tuček, P. Jakubec, J. Kašlík, I. Medřík, H. Tokoro, et al., Magnetic ground state of nanosized β -Fe₂O₃ and its remarkable electronic features, *RSC*

Adv. 5 (2015) 49719–49727. doi:10.1039/C5RA07484C.

- [48] X. Shi, S.L. Bernasek, A. Selloni, Formation, Electronic Structure, and Defects of Ni Substituted Spinel Cobalt Oxide: a DFT+U Study, *J. Phys. Chem. C.* 120 (2016) 14892–14898. doi:10.1021/acs.jpcc.6b03096.
- [49] A. Gupta, U. V. Waghmare, M.S. Hegde, Correlation of Oxygen Storage Capacity and Structural Distortion in Transition-Metal-, Noble-Metal-, and Rare-Earth-Ion-Substituted CeO₂ from First Principles Calculation, *Chem. Mater.* 22 (2010) 5184–5198. doi:10.1021/cm101145d.
- [50] A.M. Deml, V. Stevanović, C.L. Muhich, C.B. Musgrave, R. O’Hayre, Oxide enthalpy of formation and band gap energy as accurate descriptors of oxygen vacancy formation energetics, *Energy Environ. Sci.* 7 (2014) 1996. doi:10.1039/c3ee43874k.
- [51] Q. Javed, F.P. Wang, M.Y. Rafique, A.M. Toufiq, Q.S. Li, H. Mahmood, et al., Diameter-controlled synthesis of α -Mn₂O₃ nanorods and nanowires with enhanced surface morphology and optical properties, *Nanotechnology.* 23 (2012). doi:10.1088/0957-4484/23/41/415603.
- [52] W. Tang, E. Sanville, G. Henkelman, A grid-based Bader analysis algorithm without lattice bias., *J. Phys. Condens. Matter.* 21 (2009) 84204. doi:10.1088/0953-8984/21/8/084204.